




Cite this: *RSC Adv.*, 2020, 10, 12689

# Facile synthesis of ternary PtPdCu alloy hexapods as highly efficient electrocatalysts for methanol oxidation†

Na Gao, Xingqiao Wu, Xiao Li, Jingbo Huang, Dongsheng Li, \* Deren Yang and Hui Zhang \*

Developing an efficient Pt-based multimetallic electrocatalyst with well-defined shapes for methanol oxidation reaction (MOR) is critical, however, it still remains challenging. Here we report a one-pot approach for the synthesis of ternary PtPdCu alloy hexapods with different compositions. Their MOR activities increased in the sequence  $\text{Pt}_2\text{PdCu}_4 < \text{Pt}_3\text{PdCu}_4 < \text{Pt}_5\text{PdCu}_5$ , and were substantially higher than that of commercial Pt/C. Specifically, the  $\text{Pt}_5\text{PdCu}_5$  hexapods exhibited the highest mass ( $0.97 \text{ mA } \mu\text{g}_{\text{Pt}}^{-1}$ ) and specific ( $7.39 \text{ mA cm}^{-2}$ ) activities towards MOR, and were 5.4 and 19.4 times higher than those of commercial Pt/C ( $0.18 \text{ mA } \mu\text{g}_{\text{Pt}}^{-1}$  and  $0.38 \text{ mA cm}^{-2}$ ), respectively. This enhancement could be probably attributed to the bifunctional mechanism and ligand effect through the addition of Cu and Pd as well as the unique dendritic structure. The better tolerance for CO poisoning also endowed the PtPdCu hexapods with superior durability relative to commercial Pt/C.

Received 1st February 2020

Accepted 21st March 2020

DOI: 10.1039/d0ra00963f

rsc.li/rsc-advances

## Introduction

In the past decades, direct methanol fuel cells (DMFCs) have received great attention as a power source for portable electronic devices because of their high energy conversion efficiency, environmental friendliness and high energy density.<sup>1–4</sup> However, the methanol oxidation reaction (MOR) at the anode of DMFCs involves multiple steps, leading to the slower reaction kinetics than electro-oxidation of hydrogen. In DMFCs, platinum (Pt) is considered as the most effective monometallic catalyst for MOR.<sup>5–7</sup> However, the high price and limited abundance of Pt severely restrict its widespread commercialization.<sup>8–12</sup> As such, it is highly desirable to synthesize Pt-based catalysts for MOR with not only the low loading of Pt, but also the enhancement in the catalytic performance.<sup>13–15</sup>

Recently, tremendous efforts have been devoted to decreasing the loading of Pt and enhancing the electrocatalytic properties. Of them, introducing a second metal (*e.g.*, Pd, Cu, Ru and Ni) alloyed with Pt is the one of the most widely used method.<sup>16–21</sup> The enhancement in the catalytic properties for MOR can be understood by bifunctional mechanism and/or ligand effect through improving the tolerance of Pt toward CO poisoning.<sup>22</sup> For example, Sun and co-workers reported the synthesis of single-crystalline dendritic  $\text{Pt}_3\text{Cu}$  nanocubes with

the mass activity being 5.2 times higher than that of commercial Pt/C for MOR.<sup>23</sup> In another study, we demonstrated the synthesis of  $\text{Pd}_3\text{Pb}/\text{Pt}_n\text{Pb}$  nanocubes, showing the excellent catalytic activities for MOR due to the low CO absorption energy by the addition of Pb.<sup>24</sup> In addition to composition optimization, controlling the structures and morphologies of Pt-based nanocrystal provides an alternative promising method to improve the catalytic properties.<sup>25–27</sup> To this end, we reported the synthesis of Ru-decorated Pt cubes and icosahedra, in which the icosahedra exposed by {111} facets exhibited the superior catalytic activity for MOR relative to the cubes enclosed with {100} facets.<sup>28</sup> Compared to monometallic and bimetallic nanocrystals, nanocrystals consisting of multimetallic components provide an extra adjustability of the composition and/or structure, and thus the optimal control over their catalytic properties. Recently, there are some reports on the synthesis of Pt-based multimetallic nanocrystals, in which the branched structures received unprecedented research interest due to their high surface area-to-volume ratio and the existence of low-coordinated sites on the surface.<sup>29–31</sup> For instance, Mu and co-workers synthesized PtRuCu alloyed hexapods by a two-step method including Stranski–Krastanov growth and galvanic replacement, showing 3.8 times higher mass activity than commercial Pt/C.<sup>32</sup> However, it is difficult to synthesize the multimetallic alloyed nanocrystals due to the huge difference in the reduction potential of each component. Significantly, the synthesis of Pt-based multimetallic nanocrystals is still challenging, especially for those with well-defined shapes prepared by a simple method.

State Key Laboratory of Silicon Materials and School of Materials Science and Engineering, Zhejiang University, Hangzhou 310027, P. R. China. E-mail: msezhanghai@zju.edu.cn; mselds@zju.edu.cn

† Electronic supplementary information (ESI) available. See DOI: 10.1039/d0ra00963f



Here we report a facile and one-pot approach for the synthesis of PtPdCu hexapods with tunable compositions. The PtPdCu hexapods exhibited the substantially enhanced catalytic properties relative to the commercial Pt/C and PtCu nanodendrites, with the Pt<sub>5</sub>PdCu<sub>5</sub> achieving the highest activity and stability towards MOR due to the synergistic effect and unique structure.

## Experimental section

### Materials and chemicals

Chloroplatinic acid hydrate (iv) (H<sub>2</sub>PtCl<sub>6</sub>·xH<sub>2</sub>O, 99.99%), palladium(II) acetylacetonate (Pd(acac)<sub>2</sub>, 99%), copper(II) acetylacetonate (Cu(acac)<sub>2</sub>, 99%), trioctylphosphine oxide (TOPO, AR) were purchased from Sigma-Aldrich. Oleylamine (OAm, 80–90%) was purchased from Aladdin. Commercial Pt/C (20 wt%) were purchased from Alfa Aesar. Benzyl alcohol (BA), dimethylformamide (DMF), ethanol, acetone, chloroform and toluene were purchased from Sinopharm Chemical Reagent. All the chemicals and materials were used as received.

### Synthesis of PtPdCu hexapods

In a standard procedure for the synthesis of Pt<sub>5</sub>PdCu<sub>5</sub> hexapods, 110 mg of TOPO was dissolved in a glass vial containing 4 mL of OAm. Meanwhile, 0.06 mmol of H<sub>2</sub>PtCl<sub>6</sub>·xH<sub>2</sub>O, 0.02 mmol of Cu(acac)<sub>2</sub> and 0.003 mmol Pd(acac)<sub>2</sub> were dissolved in 4 mL of DMF. After that, the DMF solution containing Pt, Cu and Pd salt precursors was mixed into the glass vial. The mixed solution was magnetically stirred for 30 min at room temperature. The reaction was maintained at 200 °C for 3 h. Finally, the product was collected by centrifugation, washed with ethanol and cyclohexane for three times. For the synthesis of Pt<sub>3</sub>PdCu<sub>4</sub> and Pt<sub>2</sub>PdCu<sub>4</sub> hexapods, the amount of H<sub>2</sub>PtCl<sub>6</sub>·xH<sub>2</sub>O was adjusted to 0.04 and 0.02 mmol, respectively, while keeping other conditions unchanged. In the absence of Pd salt precursors, PtCu nanodendrites were generated.

### Morphological, structural, and compositional characterizations

Transmission electron microscopy (TEM) images of the obtained samples were taken using a HITACHI HT-7700 microscope operated at 100 kV. The X-ray diffraction (XRD) patterns were recorded on a Miniflex 600 X-ray diffractometer in a scan range of 10–80° at a scan rate of 10° min<sup>−1</sup>. High-resolution transmission electron microscopy (HRTEM), high-angle annular dark-field scanning TEM (HAADF-STEM) and Energy Dispersive X-ray (EDX) mapping analyses were performed using a FEI Tecnai F20 G2 microscope operated at 200 kV. X-ray photoelectron spectrometer (XPS) was performed on ESCALAB 250Xi (Thermo, U.K.). The corresponding binding energies were calibrated with a C–C 1s peak of 284.5 eV. The atomic ratios of Pd, Pt and Cu in these samples were determined using inductively coupled plasma atomic emission spectrometry (ICP-AES, IRIS Intrepid II XSP, TJA Co., USA).

### Electrochemical measurement

Electrochemical measurements were carried out in a three-electrode system at room temperature using a rotating disk electrode (RDE, Pine Research Instrumentation, USA) connected to an electrochemical workstation (CHI 760E). A reversible hydrogen electrode (RHE) was used as the reference. The counter electrode was a Pt wire. To make catalyst ink, 5 mg of PtPdCu/C or Pt/C catalysts were dispersed in 5 mL of a mixed solvent and sonicated for 10 min. The solvent contained a mixture of de-ionized water, isopropanol, and 5% Nafion 117 solution at the volumetric ratio of 8 : 2 : 0.05. 20 μL of the PtPdCu/C or Pt/C catalyst ink was added onto the RDE and dried under an air flow to make the working electrode. The geometric area of each RDE was 0.196 cm<sup>2</sup>. The electrochemical active surface area (ECSA) was determined from the cyclic voltammogram (CV) curves, calculating the amount of charges by integrating the hydrogen desorption region after double layer correction. The CV measurement was performed in Ar-saturated 0.1 M HClO<sub>4</sub> solution at room temperature with a sweep rate of 50 mV s<sup>−1</sup>. For the electrooxidation of methanol, CV curves were recorded in an Ar-purged 0.5 M H<sub>2</sub>SO<sub>4</sub> and 0.5 M CH<sub>3</sub>OH solution at a sweep rate of 50 mV s<sup>−1</sup>. Chronoamperometric measurements of methanol oxidation were obtained in an Ar-purged 0.5 M H<sub>2</sub>SO<sub>4</sub> and 0.5 M CH<sub>3</sub>OH solution at the front peak positions of the forward curve for 1000 s (the holding voltage is 0.68, 0.69, 0.71, and 0.63 V for the Pt<sub>2</sub>PdCu<sub>4</sub>, Pt<sub>3</sub>PdCu<sub>4</sub>, Pt<sub>5</sub>PdCu<sub>5</sub> hexapods and Pt/C, respectively).

## Results and discussion

The PtPdCu hexapods were generated by the reduction of H<sub>2</sub>PtCl<sub>6</sub>·xH<sub>2</sub>O, Cu(acac)<sub>2</sub> and Pd(acac)<sub>2</sub> in a mixture of OAm and

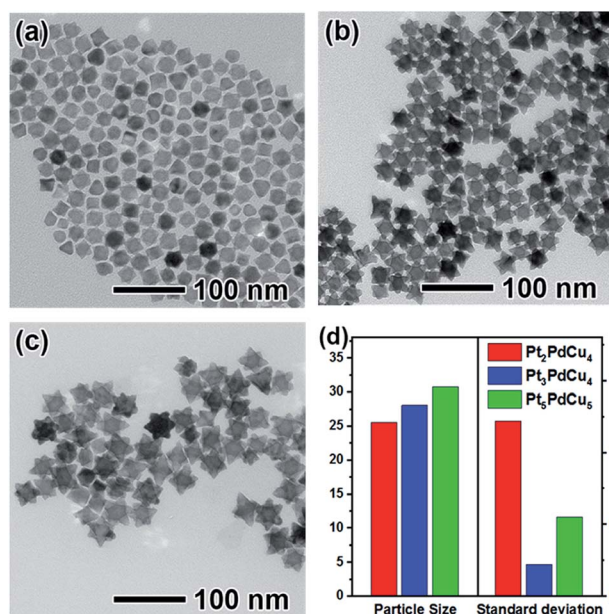


Fig. 1 (a–c) TEM images and (d) size distributions of the PtPdCu hexapods prepared using the standard procedure by varying the amount of Pt salt precursors from 0.02 to 0.04 and 0.06 mmol, respectively.



DMF containing TOPO at 200 °C. Fig. 1a–c shows TEM images of the PtPdCu nanocrystals prepared by varying the amount of Pt salt precursors. It is clear that most of the nanocrystals have a hexapod shape with the uniform size. The atomic ratio of Pt/Pd/Cu was determined by the ICP-AES analysis (Table S1†). Based on the ICP-AES data, these three PtPdCu hexapods were labelled as Pt<sub>5</sub>PdCu<sub>5</sub>, Pt<sub>3</sub>PdCu<sub>4</sub> and Pt<sub>2</sub>PdCu<sub>4</sub>, respectively. We randomly selected 100 particles to calculate the average sizes of these PtPdCu hexapods, as shown in Fig. 1d and S1.† As can be seen, the average sizes of the Pt<sub>5</sub>PdCu<sub>5</sub>, Pt<sub>3</sub>PdCu<sub>4</sub> and Pt<sub>2</sub>PdCu<sub>4</sub> hexapods are 31.80, 28.08 and 25.56 nm, respectively. In addition, the length of the pods increases with the amount of Pt salt precursors. Fig. S2† shows the XRD patterns of such three samples. As observed, there are three main diffraction peaks corresponding to the (111), (200) and (220) planes of a face-centered cubic (fcc) structure, confirming the formation of the alloyed phase. In addition, the diffraction peaks gradually shift to higher angles with decreasing the amount of Pt as compared to the standard data of pure Pt due to the alloying of Pt with smaller Pd and Cu atoms.

The morphology, structure and composition of the Pt<sub>5</sub>PdCu<sub>5</sub> hexapods were further characterized by the HAADF-STEM, HRTEM, EDX mapping and line-scan analyses, as shown in Fig. 2. Clearly, the HAADF-STEM image (Fig. 2a) confirms the formation of hexapods. The typical HRTEM image (Fig. 2b) of an individual hexapod shows well-resolved, ordered fringes in the same orientation, indicating that the hexapod is a single crystal. The fringes with lattice spacing of 2.34 and 1.98 Å can be indexed to the {111} and {200} planes of PtPdCu alloy with an fcc structure, respectively. The fringes corresponding to the {200} facets are perpendicular to longitudinal orientation of the pod, suggesting the preferential overgrowth of the pod along <100> direction marked by an arrow. The distribution of Pt, Pd and Cu

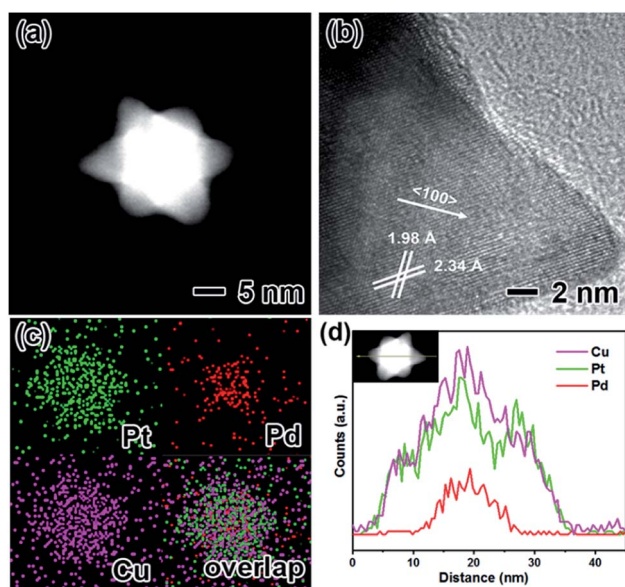


Fig. 2 Morphological, structural, and compositional characterizations of the Pt<sub>5</sub>PdCu<sub>5</sub> hexapods: (a) HAADF-STEM image, (b) HRTEM image, (c) EDX mapping images, and (d) line-scan profiles.

in the hexapod is determined using EDX analysis (Fig. 2c and d). Clearly, Pd is concentrated in the interior, while Pt and Cu distribute throughout the hexapod (Fig. 2c). This demonstration is further supported by the EDX line-scan spectra (Fig. 2d). As such, the interior of the hexapod is Pd rich, while the surface is Pt and Cu rich. In addition, the Pt<sub>3</sub>PdCu<sub>4</sub> (Fig. S3†) and Pt<sub>2</sub>PdCu<sub>4</sub> hexapods (Fig. S4†) were also characterized by HRTEM, HAADF-STEM, and EDX mapping and line-scan analyses, showing the similar result except for the length of pods.

In order to reveal the formation mechanism of the PtPdCu hexapods, the evolution of their morphology and composition with the reaction time are systematically investigated. For simplicity, the Pt<sub>5</sub>PdCu<sub>5</sub> hexapods were selected as a typical example. A series of samples in the synthesis of the Pt<sub>5</sub>PdCu<sub>5</sub> hexapods were taken from the reacting solution at different reaction time for TEM and ICP-AES characterizations, as shown in Fig. 3 and S5,† respectively. In the initial stage of the reaction ( $t = 10$  min), a rich variety of small nanoparticles were obtained (Fig. 3a). The ICP-AES data (Fig. S5†) show that these particles are mainly composed of Pd and Cu with the total atomic percentage more than 90%. It is indicated that Pd is alloyed with Cu before Pt due to the higher redox potential of Pd<sup>2+</sup>/Pd

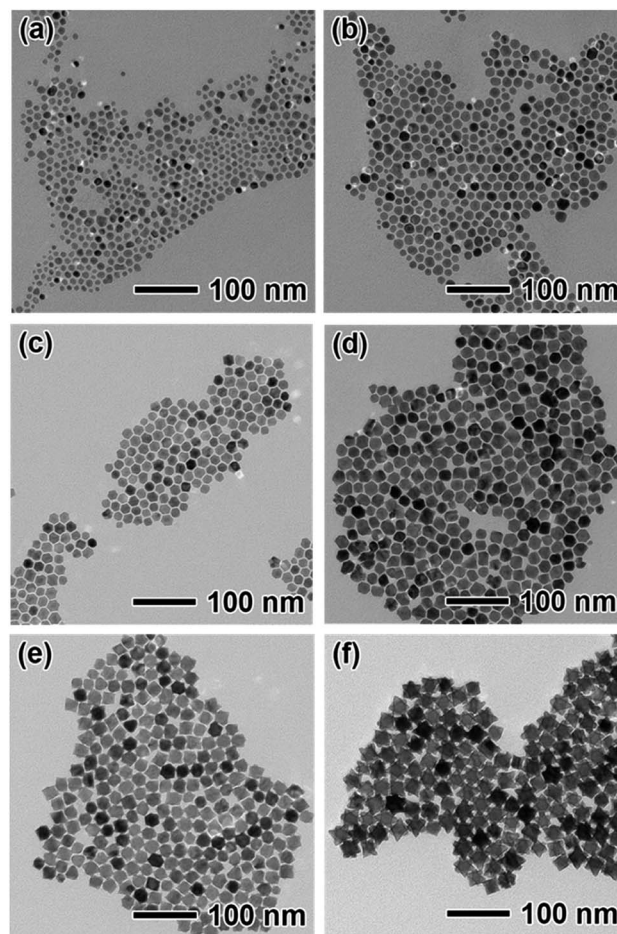


Fig. 3 TEM images of the PtPdCu nanocrystals prepared using the standard procedure, except for the different periods of time: (a) 10 min, (b) 15 min, (c) 30 min, (d) 45 min, (e) 1 h and (f) 2 h.



(0.951 V *versus* RHE) than that of  $\text{PtCl}_4^{2-}/\text{Pt}$  (0.755 V *versus* RHE). With extension of the reaction time ( $t = 15\text{--}45$  min, Fig. 3b–d), these small nanoparticles gradually grew up and evolved into truncated octahedra. During the reactions, the atomic ratio of Pt increased dramatically, even higher than that of Pd at 45 min due to the higher feeding ratio of Pt salt precursors (Fig. S5†). As the reaction was continued to  $t = 1$  h (Fig. 3e), the tiny pods started to protrude out from six {100} facets of each truncated octahedron due to the preferential overgrowth along the <100> directions, which is in consistent with the previous report.<sup>33</sup> When the reaction time reached 2 h (Fig. 3f), high quality hexapods were generated with the continue preferential overgrowth. As such, the formation of the hexapods involved in two steps including the initial formation of the truncated octahedra and then preferential overgrowth of the pods with the truncated octahedra as the seeds. The formation of the truncated octahedra is easy to be understood since this shape is the thermodynamically stable structure.<sup>34</sup> Meanwhile, the formation of the truncated octahedra consumes most of the Pd salt precursors. The subsequent growth of the nanocrystals follows up the dendritic growth behavior of PtCu. A control experiment without  $\text{Pd}(\text{acac})_2$  was performed to confirm such dendritic growth. From Fig. S6,† the PtCu dendritic nanocrystals were generated in the absence of  $\text{Pd}(\text{acac})_2$ . As such, the hexapods were formed through the preferential overgrowth of the pods with the truncated octahedra as the seeds.

The valence and electronic states of three PtPdCu hexapods were analyzed using the XPS technique, as shown in Fig. S7.† Since the surface of the hexapods is dominated by Pt and Cu, we only discuss the variation of Pt 4f and Cu 2p for simplicity (Table S2†). As observed, Pt and Cu elements exist in both zero-valent and divalent states for these three samples, with the metallic state being the majority. In addition, there is an obvious shift of Pt 4f and Cu 2p peaks in these three hexapods compared to those of the corresponding bulk materials. Taking  $\text{Pt}_5\text{PdCu}_5$  hexapods as an example (Fig. S7a†), the binding energies of  $\text{Pt}^0$  locate at 70.81 ( $4f_{7/2}$ ) and 73.99 ( $4f_{5/2}$ ) eV, respectively, which display a negative shift of  $\sim 0.4$  eV compared with bulk Pt 4f peaks at 71.20 ( $4f_{7/2}$ ) and 74.53 eV ( $4f_{5/2}$ ). On the contrary, there is a positive shift of the binding energies of  $\text{Cu}^0$  in the  $\text{Pt}_5\text{PdCu}_5$  hexapods (Fig. S7b†) with the peaks locating at 932.0 ( $2p_{3/2}$ ) and 951.8 eV ( $2p_{1/2}$ ) compared to the standard data of bulk Cu (931.7 and 951.5 eV). As such, these results demonstrated that the electronic structure of Pt was modulated with incorporation of Cu through the electron coupling between them because of their different work function (*i.e.*, ligand effect).<sup>35,36</sup> This effect might weaken the adsorption of partial oxidation intermediates (*e.g.*, CO) on Pt, thereby improving the catalytic activity for MOR by alleviating the CO poisoning.<sup>37–39</sup>

These three hexapods were loaded on carbon support (Vulcan XC-72R, Fig. S8†), and then evaluated as the catalysts for MOR with commercial Pt/C as a reference. Fig. S9† shows the cyclic voltammetry (CV) curves of these four catalysts including commercial Pt/C recorded in Ar-purged 0.1 M  $\text{HClO}_4$  solutions at a sweep rate of  $50 \text{ mV s}^{-1}$ . As determined by the hydrogen desorption region (0.05–0.4 V) in the CV, the electrochemically

active surface areas (ECSAs) of the  $\text{Pt}_2\text{PdCu}_4$ ,  $\text{Pt}_3\text{PdCu}_4$  and  $\text{Pt}_5\text{PdCu}_5$  hexapods are 12.2, 11.1 and  $13.2 \text{ m}^2 \text{ g}_{\text{Pt}}^{-1}$ , respectively, which is smaller than that of Pt/C ( $46.7 \text{ m}^2 \text{ g}_{\text{Pt}}^{-1}$ ), probably due to their larger particle size (Table S3†). Fig. 4a and b compare the CV curves of these four catalysts for MOR performed in the solution containing 0.5 M  $\text{H}_2\text{SO}_4$  and 0.5 M  $\text{CH}_3\text{OH}$  at a sweep rate of  $50 \text{ mV s}^{-1}$ . Obviously, the hexapods exhibited higher specific and mass activities relative to the commercial Pt/C due to their unique hexapod structure and synergetic effect of multiple components. In addition, the MOR activities of the hexapods followed the sequence:  $\text{Pt}_2\text{PdCu}_4 < \text{Pt}_3\text{PdCu}_4 < \text{Pt}_5\text{PdCu}_5$ . Specifically, the  $\text{Pt}_5\text{PdCu}_5$  hexapods showed the highest mass ( $0.97 \text{ mA } \mu\text{g}_{\text{Pt}}^{-1}$ ) and specific ( $7.39 \text{ mA cm}^{-2}$ ) activities towards MOR, which are 5.4 and 19.4 times higher than the commercial Pt/C ( $0.18 \text{ mA } \mu\text{g}_{\text{Pt}}^{-1}$  and  $0.38 \text{ mA cm}^{-2}$ ), respectively (Fig. 4c). For comparison, the PtCu nanodendrites were also evaluated as electrocatalysts towards MOR in the acid media, as shown in Fig. S10.† As observed, the PtPdCu hexapods exhibited better catalytic properties for MOR relative to the PtCu nanodendrites, indicating the critical role of Pd in the electrocatalysts. Table S4† summarizes the specific and mass activities of the  $\text{Pt}_5\text{PdCu}_5$  hexapods in this work and state of art electrocatalysts in literatures. Clearly, the  $\text{Pt}_5\text{PdCu}_5$  hexapods outperformed over most of the previously reported Pt-based electrocatalysts in acid media. The superior catalytic activities of the hexapods can be understood by the bifunctional mechanism and ligand effect.<sup>40,41</sup> As well-known, Pt is the active site for methanol adsorption and dissociation during MOR, resulting in the formation of intermediates mainly containing  $\text{CO}_{\text{ads}}$ . Such  $\text{CO}_{\text{ads}}$  intermediates can severely poison these active sites of Pt through strong adsorption, and eventually deactivate Pt-based electrocatalysts. The incorporation of Cu

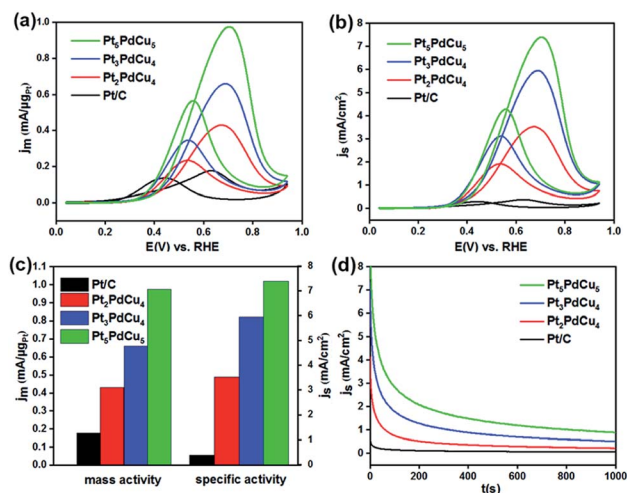


Fig. 4 (a and b) Cyclic voltammograms (CVs) of four different catalysts including  $\text{Pt}_5\text{PdCu}_5$  hexapods (green),  $\text{Pt}_3\text{PdCu}_4$  hexapods (blue),  $\text{Pt}_2\text{PdCu}_4$  hexapods (red) and commercial Pt/C (black) for the MOR normalized by the ECSA and Pt mass, respectively. (c) Specific and mass activity at the peak position of the forward curve. (d) Current–time curves ( $I-t$ ) for methanol electrooxidation of these four catalysts at the peak position voltage (vs. RHE) for 1000 s.



and Pd can cause a down shift of d band center of Pt (ligand effect),<sup>42</sup> thereby reducing its binding strength with the adsorbed intermediates (e.g., CO) and enhancing the tolerance to the CO poisoning. The addition of Cu and Pd with the oxyphile capability also promotes the removal of CO<sub>ads</sub> intermediates during the catalytic reaction, and thus substantially enhances the activity by inhibiting the CO poisoning (bifunctional mechanism).<sup>43</sup> In addition, the hexapods usually contains some low-coordinated sites on the surface of pods, which was demonstrated in our previous report on Pd@Pt hexapods.<sup>44</sup> These low-coordinated sites are active for MOR, which might be responsible for the better MOR activity with the increase in the length of pods (Pt<sub>2</sub>PdCu<sub>4</sub> < Pt<sub>3</sub>PdCu<sub>4</sub> < Pt<sub>5</sub>PdCu<sub>5</sub>). The electrocatalytic stability of these four catalysts for MOR was investigated by long-term current (*I*-*t*) measurement technique, as shown in Fig. 4d. As can be seen, the hexapods show the higher steady current density relative to the commercial Pt/C for MOR over the entire time range (1000 s), indicating the superior stability. Such superior durability can be attributed to weaker CO adsorption on the hexapods and better CO tolerance due to the incorporation of Cu and Pd.

## Conclusions

In summary, we have developed a facile approach to synthesize the PtPdCu hexapods with tunable compositions. Such hexapods were generated through two steps including the initial formation of thermodynamically stable truncated octahedra in combination with the subsequent preferential overgrowth from six {100} facets of truncated octahedra. The hexapods exhibited the substantially enhanced catalytic activity and stability for MOR relative to the commercial Pt/C and PtCu nanodendrites with the Pt<sub>5</sub>PdCu<sub>5</sub> hexapods being the best one. This enhancement can be probably attributed to the bifunctional mechanism and ligand effect through the incorporation of Cu and Pd as well as the unique dendritic structure. This work not only provides a facile method to the synthesis of PtPdCu alloyed nanostructures with well-defined shapes, but also offers a great opportunity to design ternary catalysts with enhanced performance for a rich variety of potential applications.

## Conflicts of interest

There are no conflicts to declare.

## Acknowledgements

Electron microscopy was carried out in the Center for Electron Microscopy of Zhejiang University. This work was supported by the National Science Foundation of China (51522103, 61721005 and 51871200) and the National Program for Support of Top-notch Young Professionals.

## Notes and references

- 1 N. V. Long, Y. Yang, M. T. Cao, N. V. Minh, Y. Cao and M. Nogami, *Nano Energy*, 2013, **2**, 636–676.

- 2 T. Cochell, W. Li and A. manthiram, *J. Phys. Chem. C*, 2013, **117**, 3865–3873.
- 3 X. Zhao, J. Zhang, L. J. Wang, H. Li, Z. Liu and W. Chen, *ACS Appl. Mater. Interfaces*, 2015, **7**, 26333–26339.
- 4 S. Jiang, B. Yi, Q. Zhao, H. Zhang, Y. Su, H. Yu and Z. Shao, *RSC Adv.*, 2016, **6**, 82370–82375.
- 5 S. F. Xue, W. T. Deng, F. Yang, J. Yang, I. S. Amiinu, D. He, H. Tang and S. Mu, *ACS Catal.*, 2018, **8**, 7578–7584.
- 6 J. Lan, K. Wang, Q. Yuan and X. Wang, *Mater. Chem. Front.*, 2017, **1**, 1217–1222.
- 7 Y. Xiong, Y. Ma, J. Li, J. Huang, Y. Yan, H. Zhang, J. Wu and D. Yang, *Nanoscale*, 2017, **9**, 11077–11084.
- 8 N. K. Chaudhari, Y. Hong, B. Kim, S. Choi and K. Lee, *J. Mater. Chem. A*, 2019, **7**, 17183–17203.
- 9 G. Xu, R. Sui, J. Liu, L. Zhang, X. Gong, R. Gao, B. Liu and J. Zhang, *J. Mater. Chem. A*, 2018, **6**, 12759–12767.
- 10 B. Lu, T. Sheng, N. Tian, Z. Zhang, C. Xiao, Z. Cao, H. Ma, Z. Zhou and S. Sun, *Nano Energy*, 2017, **33**, 65–71.
- 11 L. Lu, S. Chen, S. Thota, X. Wang, Y. Wang, S. Zou, J. Fan and J. Zhao, *J. Phys. Chem. C*, 2017, **121**, 19796–19806.
- 12 B. Jiang, C. Li, V. Malgras and Y. Yamauchi, *J. Mater. Chem. A*, 2015, **3**, 18053–18058.
- 13 F. Wu, J. Lai, L. Zhang, W. Niu, B. Lou, R. Luque and G. Xu, *Nanoscale*, 2018, **10**, 9369–9375.
- 14 G. Fu, H. Liu, N. You, J. Wu, D. Sun, L. Xu, Y. Tang and Y. Chen, *Nano Res.*, 2016, **9**, 755–765.
- 15 Y. Kuang, Z. Cai, Y. Zhang, D. He, X. Yan, Y. Bi, Y. Li, Z. Li and X. Sun, *ACS Appl. Mater. Interfaces*, 2014, **6**, 17748.
- 16 J. Park, M. K. Kabiraz, H. Kwon, S. Park, H. Baik, S. Choi and K. Lee, *ACS Nano*, 2017, **11**, 10844–10851.
- 17 M. Tang, S. Luo, K. Wang, H. Du, R. Sripathoorat and P. Shen, *Nano Res.*, 2018, **11**, 4786–4795.
- 18 A. Yin, X. Min, W. Zhu, W. Liu, Y. Zhang and C. Yan, *Chem. - Eur. J.*, 2012, **18**, 777–782.
- 19 X. Huang, Z. Zhao, Y. Chen, E. Zhu, M. Li, X. Duan and Y. Huang, *Energy Environ. Sci.*, 2014, **7**, 2957–2962.
- 20 R. Sripathoorat, K. Wang, S. Luo, M. Tang, H. Du, X. Du and P. Shen, *J. Mater. Chem. A*, 2016, **4**, 18015–18021.
- 21 S. Wang, W. Zhu, J. Ke, J. Gu, A. Yin, Y. Zhang and C. Yan, *Chem. Commun.*, 2013, **49**, 7168–7170.
- 22 J. Tiwari, R. Tiwari, G. Singh and K. Kim, *Nano Energy*, 2013, **2**, 553–578.
- 23 Y. Kuang, Y. Zhang, Z. Cai, G. Feng, Y. Jiang, C. Jin, J. Luo and X. Sun, *Chem. Sci.*, 2015, **6**, 7122–7129.
- 24 X. Wu, Y. Jiang, Y. Yan, X. Li, S. Luo, J. Huang, J. Li, R. Shen, D. Yang and H. Zhang, *Adv. Sci.*, 2019, **6**, 1902249.
- 25 L. Huang, W. Zhang, P. Li, Y. Song, H. Sheng, Y. Du, Y. Wang, Y. Wu, X. Hong, Y. Ding, X. Yuan and M. Zhu, *Nano Res.*, 2019, **12**, 1147–1153.
- 26 H. Wang, S. Yin, Y. Xu, X. Li, A. Alsheri, Y. Yamauchi, H. Xue, Y. Kaneti and L. Wang, *J. Mater. Chem. A*, 2018, **6**, 8662–8668.
- 27 Y. Jia, J. Su, Z. Chen, K. Tan, Q. Chen, Z. Cao, Y. Jiang, Z. Xie and L. Zheng, *RSC Adv.*, 2015, **5**, 18153–18158.
- 28 Z. Lin, W. Chen, Y. Jiang, T. Bian, H. Zhang, J. Wu, Y. Wang and D. Yang, *Nanoscale*, 2016, **8**, 12812–12818.
- 29 Y. Lee, M. Im, J. Hong and S. Han, *ACS Appl. Mater. Interfaces*, 2017, **9**, 44018–44026.



- 30 H. An, Z. Zhao, Q. Wang, L. Zhang, M. Gu and C. Li, *ChemElectroChem*, 2018, **5**, 1345–1349.
- 31 H. Li, C. Cui, S. Zhao, H. Yao, M. Gao, F. Fan and S. Yu, *Adv. Energy Mater.*, 2012, **2**, 1182–1187.
- 32 S. Xue, W. Deng, F. Yang, J. Yang, I. S. Amiin, D. He, H. Tang and S. Mu, *ACS Catal.*, 2018, **8**, 7578–7584.
- 33 W. Niu, L. Zhang and G. Xu, *ACS Nano*, 2010, **4**, 1987–1996.
- 34 Y. Xia, Y. Xiong, B. Lim and S. Skrabalak, *Angew. Chem., Int. Ed.*, 2009, **48**, 60–103.
- 35 D. Chen, P. S. H. Liu and J. Yang, *J. Mater. Chem. A*, 2017, **5**, 4421–4429.
- 36 B. Tan and Y. Wu, *J. Phys. Chem. B*, 2006, **110**, 15932–15938.
- 37 Y. Fan, Y. Zhang, Y. Cui, J. Wang, M. Wei, X. Zhang and W. Li, *RSC Adv.*, 2016, **6**, 83373–83379.
- 38 G. Wang, B. Huang, L. Xiao, Z. Ren, H. Chen, D. Wang, H. Abruña, J. Lu and L. Zhuang, *J. Am. Chem. Soc.*, 2014, **136**, 9643–9649.
- 39 L. Dai, S. Mo, Q. Qin, X. Zhao and N. Zheng, *Small*, 2016, **12**, 1572–1577.
- 40 H. Gasteiger, N. Markovic, P. Ross and E. Cairns, *J. Phys. Chem.*, 1993, **97**, 12020–12029.
- 41 J. Greeley and M. Mavrikakis, *Catal. Today*, 2006, **111**, 52–58.
- 42 Y. Xiong, H. Shan, Z. Zhou, Y. Yan, W. Chen, Y. Yang, Y. Liu, H. Tian, J. Wu, H. Zhang and D. Yang, *Small*, 2017, **13**, 1603423.
- 43 N. Kakati, J. Maiti, S. Lee, S. Lee, S. Jee, B. Viswanathan and Y. Yoon, *Chem. Rev.*, 2014, **114**, 12397–12429.
- 44 Y. Xiong, Y. Ma, J. Li, J. Huang, Y. Yan, H. Zhang, J. Wu and D. Yang, *Nanoscale*, 2017, **9**, 11077–11084.

